Explaining the Broad Raman Peak for Alkynes Solvated in Triethylamine

Authors:

Anagha Aneesh
Kristina Streu
Clyde A. Daly Jr. (corresponding author)

Abstract

The terminal alkyne C≡C stretch has a large Raman scattering cross section in the "silent" region for biomolecules. Experimental work taking advantage of this property provide an impetus for the development of theoretical tools addressing the vibration. In prior work, we have developed a localized normal mode method for computing terminal alkyne vibrational frequencies using a discrete variable representation of the potential energy surface. Using this method and molecular dynamics simulations, we interpret the unusually broad Raman spectrum of alkynes solvated in triethylamine. Energy decomposition analysis is performed on alkyne-triethylamine dimers to determine that like charge transfer, electrostatics, and Pauli exclusion have large effects on the frequency. Molecular dynamics simulations are performed and uncover that the terminal alkyne hydrogen interacts strongly with the triethylamine nitrogen when the alkynes are solvated in triethylamine. Using this data, a spectroscopic map for terminal alkynes in triethylamine is developed and used to compute Raman spectra. We find that the broad experimental spectra result from the combination of a population of alkynes associated with the solvent nitrogens and a population not associated with those nitrogens. This work sets the stage for investigations of alkynes in more complex environments.

Introduction

Infrared and Raman spectroscopy are effective tools for understanding the structure and dynamics of complex condensed phase systems.[1–3] The interpretation of these spectra can be aided by the use of vibrational probes.[4–6] A good probe exhibits reliable changes in its spectrum in response to specific changes in their environment. For example, OH and OD groups report on the propensity of the system to donate or accept hydrogen bonds. When donating a hydrogen bond, the OH or OD frequency decreases; when accepting a hydrogen bond, adjacent OH or OD frequencies increase.[7] Terminal alkynes, which absorb weakly in the IR but have strong Raman signals, have recently been explored as possible vibrational probes.[8–12] They have already been used as tags to investigate some biochemical problems due to their small size, biorthogonality,

and strong peak in the transparent window of Raman spectra (1800-2600 cm^{-1}).[13] Tagging studies are focused on detecting the presence of the functional group and whatever object it is attached to. However, to use alkynes as a probe, the specific environmental factors that contribute to changes in frequency must be carefully determined, if there are any.

In a recent paper, Romei et al. experimentally determined the Raman scattering of two terminal alkyne molecules in a variety of solvents to with the aim of developing the terminal alkyne as a new probe group.[8] One of the most interesting results of this study was for triethylamine (TEA). The C≡C-H stretch Raman peaks were particularly wide and seemed to be made from two subpeaks. One subpeak had a significantly lower center frequency than the other. Raman spectra of the same alkynes in other solvents did not show this two-peak behavior. However, the center frequencies of alkynes in some solvents were lower than either TEA-solvent subpeak, while center frequencies for alkynes in some other solvents were higher than either TEA-solvent subpeak. Roughly, solvents where alkynes had lower center frequencies tended to have more Lewis basic environments, and higher frequencies were related to electron poor environments (though there were significant exceptions to this rule). Tentatively, the researchers proposed that there are two subpopulations – one where the alkyne is in an electron rich environment, and one where the alkyne is in an electron poor environment. However, the lack of clarity in these trends in the other solvents clouds this picture. We aim to clarify the origin of the subpeaks in the experimental Raman spectra of alkynes in TEA using computational chemistry methods.

In this work, we use density functional theory (DFT) calculations, molecular dynamics (MD) simulations, and our recently developed localized normal mode discrete variable representation (LNM-DVR) vibrational method to determine the molecular origin of these Raman peaks.[14] We focus on the same molecules as were used in the experiments, 4-ethynylbenzyl alcohol and propargyl acetate. From MD, we find that the alkyne triple bond moiety can occupy two environments: one where it faces the nitrogen in TEA, and one where it faces the ethyl groups. It moves between these environments relatively slowly. From DFT, we find that the frequency changes substantially between these two environments and that a combination of electrostatic effects, charge transfer, and Pauli repulsion is the cause of most of this change. Finally, we extract snapshots from MD simulations of the alkynes in TEA and use LNM-DVR to calculate the contribution to the C≡C-H stretch vibrational frequency due to the solvent. We develop a spectroscopic map by fitting these frequencies to the electric field near the terminal alkyne and the repulsive portion of the Lennard-Jones potential. Using this spectroscopic map, we compute Raman spectra. We find that these computed spectra are asymmetric in a similar way to the experiment. Overall, we are able to confirm that, at least in TEA, the alkyne vibration reports most strongly on the electron density of its environment.

Methods

Dimer Frequency Calculations: All density functional theory (DFT) calculations were performed in Q-Chem 5.4 using B3LYP-D3/def2-TZVPD, TPSS-D3/6-311++G**, and PBEh-3c/def2-mSVP.[15–20] We investigated the interactions of two terminal alkyne molecules with triethylamine (TEA); these were 4-ethynylbenzyl alcohol (EBA) and propargyl acetate (PAC). Initial structures of these molecules interacting with a single TEA molecule were obtained from a MD simulation (described below). The dimer geometries were optimized to a maximum gradient

of 3 x 10⁻⁶ atomic units. If this was not possible, the gradient was instead optimized to a maximum of 30 x 10⁻⁶ atomic units. We constrained the TEA nitrogen to terminal hydrogen distance to 20 evenly spaced values between about 2 Å (the optimized structure with no constraints) and about 11.65 Å (enough distance that the two molecules were no longer interacting). The structures were optimized under these distance constraints. The LNM-DVR method developed in previous work was used to compute the anharmonic frequency for the C≡C-H stretch vibration at each geometry.[14,21] In this way, we obtained anharmonic normal mode frequencies across an array of nitrogen-hydrogen distances.

DVR-Based Frequency Decomposition Analysis: The goal of a vibrational DVR calculation is to construct the Hamiltonian matrix, H, for a particular vibration in a grid point position basis and then diagonalize it. The grid is formed along a vibrational coordinate, Q, with P points $Q_1, Q_2, Q_3, \dots Q_P$ equally spaced by ΔQ. The elements of the Hamiltonian matrix are given by,

$$H_{ij} = T_{ij} + V(Q_i)\delta_{ij} \tag{1}$$

The values i and j index the grid points from 1 to the total number of grid points P, which in this case was always 20. $V(Q)$ is the Born-Oppenheimer PES for the vibration, which is a function of the vibrational coordinate Q. The elements of the kinetic energy operator, T, are given in atomic units by,

$$T_{ij} = \frac{(-1)^{i-j}}{2\mu_Q \Delta Q^2} \begin{cases} \dfrac{\pi^2}{3}, & i = j \\ \dfrac{2}{(i-j)^2}, & i \neq j \end{cases} \tag{2}$$

where μ_Q is the reduced mass of the vibration.[14,21] Once the Hamiltonian matrix is constructed, it can be diagonalized. This returns eigenvectors which are interpreted as wavefunctions and eigenvalues which are interpreted as energy levels. The vibrational frequency we are interested in can be found by taking the difference between the two lowest energy levels, given by,

$$\omega = \frac{E_1 - E_0}{\hbar} \tag{3}$$

To determine the effect of charge transfer, polarization, and frozen orbital interactions on the vibrational frequencies, we manipulated the PESs used in our DVR method. For each molecular geometry composing a vibrational grid, we apply energy decomposition analysis based on absolutely localized molecular orbitals (ALMO).[22] The terminal alkyne molecule (PAC or EBA) was treated as one fragment and the TEA molecule was treated as another; each fragment was assumed to be neutrally charged. The ALMO calculations were performed across the vibrational coordinate, allowing us to decompose the full vibrational PES into terms representing the potential energy of the isolated molecules (ISO), electrostatics (ELEC), Pauli repulsion (PAULI), dispersion (DISP), the polarization energy (POL), and charge transfer (CT),

$$V(Q) = V_{\text{ISO}}(Q) + \Delta E_{\text{ELEC}}(Q) + \Delta E_{PAULI}(Q) + \Delta E_{DISP}(Q) + \Delta E_{\text{POL}}(Q) + \Delta E_{\text{CT}}(Q) \qquad (4)$$

The isolated potential energy, $V_{\text{ISO}}(Q)$, is the energy the system would have if the fragments were infinitely separated. The frozen orbital interaction, $\Delta E_{\text{FRZ}}(Q) = \Delta E_{\text{ELEC}}(Q) + \Delta E_{PAULI}(Q) + \Delta E_{DISP}(Q)$, describes the energy change upon bringing the molecules together without allowing the molecular orbitals to change from their isolated configurations. This energy term can be broken down into contributions from permanent electrostatics, $\Delta E_{\text{ELEC}}(Q)$, Pauli repulsion, $\Delta E_{PAULI}(Q)$, and dispersion, $\Delta E_{DISP}(Q)$. The polarization energy contribution, $\Delta E_{\text{POL}}(Q)$, arises from the *intramolecular* relaxation of the orbitals of each molecule in the presence of the other molecule and its orbitals. Finally, the charge transfer energy, $\Delta E_{\text{CT}}(Q)$, describes the energy change when the orbitals are finally allowed to mix between the fragments and so the full Born-Oppenheimer potential energy surface, $V(Q)$, is recovered.[23] These interaction energies can be incorporated into the DVR procedure described above to obtain the effect of these interactions on the vibrational frequencies. First, we construct a Hamiltonian where a selected effect has been removed

$$H_{m-\text{REM},ij} = T_{ij} + \left[V_{\text{ISO}}(Q_i) + \sum_{n \neq m} \Delta E_n(Q_i) \right] \rightarrow \omega_{m-\text{REM}} \qquad (5)$$

where m is the interaction that we would like to remove and n iterates over all the ALMO interactions. When this Hamiltonian is diagonalized, we obtain the frequency that would be obtained if interaction m were not present, $\omega_{m-\text{REM}}$. This frequency can then be compared to the frequency obtained when all effects are included in the Hamiltonian, ω_{FULL}, to obtain the frequency change due to m, $\Delta\omega_m$,

$$H_{\text{FULL},ij} = T_{ij} + \left[V_{\text{ISO}}(Q_i) + \sum_{n} \Delta E_n(Q_i) \right] \delta_{ij} \rightarrow \omega_{\text{FULL}} \qquad (6)$$

$$\Delta\omega_m = \omega_{\text{FULL}} - \omega_{m-\text{REM}} \qquad (7)$$

Isotropic Transition Polarizabilities: The DVR method provides vibrational wavefunctions which can be used to compute matrix elements of any operator which can be defined and computed along the normal mode coordinate, Q. The transition polarizability α_{01} is defined as the matrix element of the polarizability operator with the ground and first excited vibrational states, given by

$$\alpha_{01} = \langle \Psi_0 | \hat{\alpha}(Q) | \Psi_1 \rangle \qquad (8)$$

where $\hat{\alpha}(Q)$ is the trace of the polarizability tensor surface along the normal mode coordinate, Q,

$$\hat{\alpha}(Q) = \frac{\hat{\alpha}_{xx}(Q) + \hat{\alpha}_{yy}(Q) + \hat{\alpha}_{zz}(Q)}{3} \qquad (9)$$

α_{01} is directly related to the intensity of Raman scattering which is observed in experiments.[24,25]

Molecular Dynamics Simulations: All molecular dynamics (MD) simulations were performed using OpenMM version 7.6.[26] The pressure in NPT simulations was kept constant using a Monte Carlo barostat adjusting the box volume isotropically every 25 timesteps, and the temperature in NPT and NVT simulations was held constant using the Nose-Hoover algorithm with a frequency for interactions with the heat bath of 1 ps^{-1}.[27,28] Initial simulation structures were obtained using PACKMOL.[29] The cubic and periodic simulation boxes were packed to near the experimental density of TEA, the solvent molecule. The lengths of all bonds involving hydrogen was held constant, allowing a timestep of 2 fs. The dispersive and electrostatic cutoff in our simulations was 1.4 nm and particle-mesh Ewald summation was used to correct long range electrostatics.[30] Because we were using the OPLS force field, Lennard-Jones parameters between unlike molecules were found using the geometric mean, i.e. $\sigma_{ij} = \sqrt{\sigma_{ii}\sigma_{jj}}$; $\varepsilon_{ij} = \sqrt{\varepsilon_{ii}\varepsilon_{jj}}$.[31] Unless otherwise mentioned, the following equilibration procedure was used for all simulations: (1) energy minimization to a maximum energy of 10 kJ/mol, (2) random initialization of atomic velocities according to the Maxwell-Boltzmann distribution at 5 K, (3) temperature increase from 5 K to 300 K in 1000 steps over 1 ns as pressure is held constant at 1 bar, (4) equilibration under NPT (300 K, 1 bar) conditions for 1 ns, (5) equilibration under NVT (300 K) conditions for 1 ns. Systems were considered to have equilibrated if their volume (in the NPT step) and if their total energy (in the NVT step) were constant on average in the last 0.5 ns of the appropriate step.

The OPLS-AA force field was used for these simulations, including the alkyne parameters from Rego et al.[31,32] LigParGen was used to generate an initial OPLS force field for each molecule.[33] The triethylamine parameters were used without adjustment, and result in a solvent density within 4 % of the experimental value. The alkyne parameters were adjusted in some cases to match Rego et al. For PAC, the terminal alkyne angle strengths for C04-C05-C06 and C05-C06-H0C were adjusted to the values found by Rego et al. (Figure 1) The H0C, C06, and C05 Lennard Jones parameters were also adjusted. Because of the aromatic ring in EBA, we were more careful in our adjustment - this moiety was not included in the set of molecules parameterized by Rego et al. The bonding parameters for the C08-C05 interaction given by LigParGen were similar to those from Rego et al., but the LigParGen parameters described a slightly shorter (by ~0.002 nm) and stronger (by ~8,000 kJ mol^{-1} nm^{-2}) bond. We believe the LigParGen parameters are more accurate in this case, since the aromatic ring would likely have the effect of strengthening the triple bond through resonance effects. Similar angle and Lennard-Jones parameters were adjusted as in the PAC case, except that the Lennard-Jones parameters for C09 were not changed from LigParGen's estimate. The LigParGen and Rego et al. parameters for C09 differed by less than 0.02 nm for σ and 0.03 kJ/mol for ε. Partial charges for the alkynes were obtained from a ChElPG analysis of each molecule using PBE0/6-31G(d,p) in Q-Chem as recommended by Rego et al.[15,17,32,34,35] Parameters not mentioned in this paragraph for EBA and PAC were identical between Rego et al. and LigParGen, or were not given in Rego et al.
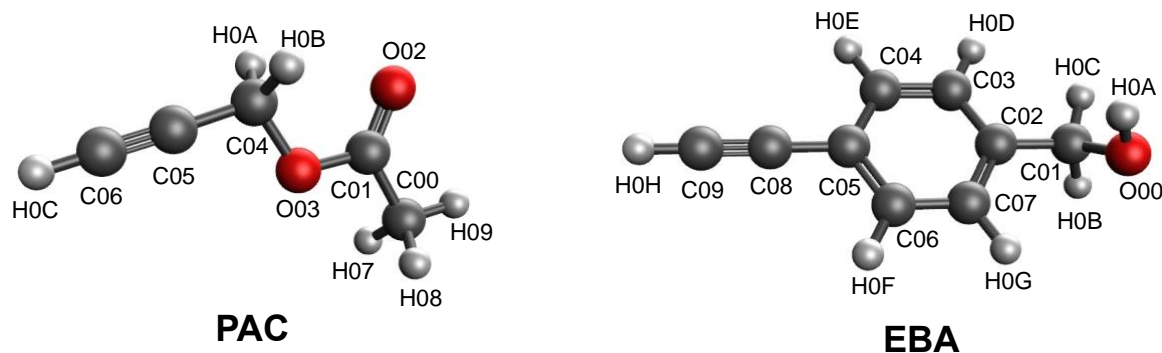
Figure 1: *Atom name assignments for PAC and EBA. For PAC (EBA), H0C (H0H) is the terminal hydrogen, C06 and C05 (C09 and C08) are the triple bonded carbons, and C04 (C05) is the first R group carbon.*

Four simulation boxes were created, each consisting of a single alkyne molecule (EBA or PAC) solvated in TEA. The initial simulation boxes were created using PACKMOL to a size of 4.2 nm x 4.2 nm x 4.2.[29] The number of TEA molecules added was roughly set to match the experimental density of TEA at 300 K, minus one molecule to make room for the alkyne. Once equilibrated simulation boxes were obtained, production simulations were performed for an additional 200 ns, collecting snapshots every 2 ps for a total of 100,000 snapshots. Simulation boxes with initial dimensions of 6.2 nm x 6.2 nm x 6.2 nm were also created and equilibrated, then run for 20 ns. 1,000 snapshots were collected from these simulations with a time separation of 20 ps for spectroscopic mapping and DFT analysis. Finally, additional 25 ns simulations with box dimensions of 6.2 nm x 6.2 nm x 6.2 nm were run where snapshots were collected every 0.1 ps in order to calculate Raman spectra.

Cylindrical Distribution Function: While the commonly used radial distribution function provides a great deal of useful information on the solvent environment experienced by an atom, it suffers from an important limitation in this case. The terminal alkyne has cylindrical symmetry but the radial coordinate is spherically symmetric. This means that the radial distribution function averages together very different environments from the point of view of the alkyne. A cylindrical distribution function (CDF) uses two coordinates and can engage more fruitfully with the alkyne's shape. To define these coordinates, we took the location of the carbon in the triple bond and connected to the R group as the origin of the coordinate system. One coordinate unit vector, $\hat{z}$, was the unit vector in the direction connecting this carbon to the other triple bonded carbon. This coordinate can be positive or negative. The other coordinate unit vector, $\hat{r}$, was the radius of a circle in the plane orthogonal to $\hat{z}$ with the same origin. This coordinate can only be positive. Using these vectors, a CDF, $g(r,z)$, can be defined as,

$$g(r,z) = \frac{\langle \rho(r,z) \rangle}{\rho} = \frac{\langle N(r,z) \rangle}{\pi(2r\Delta r^2 + \Delta r^3)\rho} \tag{10}$$

Where z and r are the CDF coordinates of an atom of interest, $\rho(r,z)$ and $N(r,z)$ are the density and number of atoms of interest at that location, respectively, ρ is the density of atoms of interest

throughout the simulation, and $\Delta r = \Delta z$ is the bin width.[36–38] $\langle ... \rangle$ indicates an average over all snapshots, counting atoms of interest within $r - \frac{\Delta r}{2} < r < r + \frac{\Delta r}{2}$ and $z - \frac{\Delta z}{2} < z < z + \frac{\Delta z}{2}$. When $g(r, z) = 1$, then the density at the indicated location is the same as it would be if the alkyne was not in solution. As both $r \to \infty$ and $z \to \infty$, we should expect $g(r, z) \to 1$ since the alkyne will have weak effects on distant parts of the solution.

Optimization of QM/MM Clusters: We selected 1,000 snapshots from our larger 6.2 nm x 6.2 nm x 6.2 nm simulation box, separated by 20 ps each. This time separation was chosen to minimize frequency correlations between the sub-selected snapshots, based on experimental estimates of the frequency correlation time in similar solvents. We find that the correlation between adjacent frequencies separated by 20 ps is quite small, less than 0.04 in absolute value. The alkyne was centered in the box, and all TEA molecules with centers of mass more than 3 nm away from the alkyne hydrogen were removed. The alkyne molecule and the nearest TEA molecule to the terminal hydrogen were included in a "quantum mechanical" (QM) region, and all other TEA molecules were included in a "molecular mechanical" (MM) region. Using Q-Chem, atoms in QM molecules were treated using DFT and atoms in MM molecules were treated as point charges, with charges given by the OPLS molecular dynamics force field.

The maximum distance of TEA molecules included in the molecular mechanics region and the number of TEA molecules included in the quantum region was determined using 10 snapshots separated by 1 ns each. Initially, all TEA molecules with centers of mass less than 3 nm away from the alkyne hydrogen were included in the MM region. To optimize the quantum region, we used our LNM-DVR method to compute the vibrational frequency when 0 through 5 TEAs were included in the QM region. The majority of the frequency shift between 0 and 5 QM TEA molecules could be captured by using 1 QM TEA molecule. Using this fixed QM region size of 1 TEA, we then reduced the maximum distance of TEA molecules included in the MM region. The frequency did not change even when the MM region was reduced to 1 nm, indicating that the 3 nm radius was converged. Because of the low cost of including MM TEA molecules, we used a maximum 3 nm cutoff for the MM region.

Molecular Effects on Frequency: The vibrational frequency from any individual snapshot can be broken down as follows,

$$\omega = \omega_g + \Delta\omega(\theta_{RCC}, \theta_{HCC}) + \Delta\omega_R + \Delta\omega_{TEA} \tag{11}$$

where ω_g is the gas phase frequency of the alkyne of interest, $\Delta\omega(\theta_{RCC}, \theta_{HCC})$ is the change to the frequency arising from bends of the internal terminal alkyne angles (since the optimum angle is 180 degrees, the dihedral only exists transiently), $\Delta\omega_R$ is the change to the frequency arising from changes to other degrees of freedom in the alkyne, and $\Delta\omega_{TEA}$ is the change to the frequency due to the TEA solvent. The effect of $\Delta\omega_R$ on the experimental spectrum will likely be overestimated by frequency calculations performed on snapshots extracted from our MD simulations. This is mainly because these degrees of freedom will, in most cases, be in their vibrational ground state. This restriction is not present in the classical MD simulation so some unlikely configurations will be sampled more than they should be. Additionally, it is extremely difficult to build a spectroscopic map which includes the 3(N-3)-6 additional degrees of freedom outside the terminal alkyne. To simplify, we assume that $\Delta\omega_R = 0$. This assumption will lead to an underestimate of the frequency

distribution, but one which we are aware of before the frequencies are even computed. Without the variance from this contribution, we expect the frequencies to consist of

$$\omega = \omega_g + \Delta\omega(\theta_{RCC}, \theta_{HCC}) + \Delta\omega_{TEA} \tag{12}$$

$\Delta\omega(\theta_{RCC}, \theta_{HCC})$ was obtained from calculations on gas phase structures of the alkynes, including constrained optimizations to specific pairs of angles. These data were fit to a smooth bivariate spline as provided in the scipy package.[39]

To obtain $\Delta\omega_{TEA}$, we performed two sets of calculations on our MD snapshots. First, we computed the frequency of the terminal alkyne from the MD simulation with one QM TEA molecule and a 3 nm radius of MM TEA solvent, which we term ω_{QM1MM3}. This can be broken down into contributions given by

$$\omega_{QM1MM3} = \omega_g + \Delta\omega_R + \Delta\omega(\theta_{RCC}, \theta_{HCC}) + \Delta\omega_{TEA} \tag{13}$$

Next, we computed the frequency for the same alkyne structures from the MD simulations, but with no QM or MM TEA molecules present. This is given the term ω_{QM0MM0} and can be broken down as

$$\omega_{QM0MM0} = \omega_g + \Delta\omega_R + \Delta\omega(\theta_{RCC}, \theta_{HCC}) \tag{14}$$

Then, $\Delta\omega_{TEA}$ is,

$$\Delta\omega_{TEA} = \omega_{QM1MM3} - \omega_{QM0MM0} \tag{15}$$

Because the alkyne structures are identical between the two calculations, ω_g, $\Delta\omega(\theta_{RCC}, \theta_{HCC})$, and $\Delta\omega_R$ all cancel in this subtraction. Since we assume $\Delta\omega_R = 0$, and we can calculate ω_g and $\Delta\omega(\theta_{RCC}, \theta_{HCC})$ separately, we can reconstruct a predicted frequency for any snapshot.

Data for Spectroscopic Mapping: To develop a spectroscopic map, we ran a 20 ns simulation where we collected snapshots every 20 ps for each alkyne, for a total of 2,000 snapshots. This collection frequency was determined based on the work of Londergan and coworkers.[8,12] We then calculated $\Delta\omega_{TEA}$ for each snapshot. To determine that 20 ps is sufficient to decorrelate the snapshots, we time ordered the frequencies and computed the correlation between snapshot frequency N and snapshot frequency N+1. This is equivalent to evaluating the frequency autocorrelation function with a time separation of 20 ps. For both alkynes the absolute value of the correlation between subsequent snapshots is less than 0.04. This data for $\Delta\omega_{TEA}$ was split into a 1,500-member training set and a 500-member test set. The alkynes were mixed together in these sets.

Computational Raman Spectra: In this work, we develop a map for $\Delta\omega_{TEA}$. Subsequently, we ran a higher resolution 25 ns simulation where snapshots were collected every 0.1 ps - frequencies were computed for each of these snapshots. The Raman spectrum was computed using the fluctuating frequency approximation

$$I(\omega) \propto \Re\left[\int_{-\infty}^{\infty} dt\, e^{i\omega t} \langle \alpha_{01}(t)\alpha_{01}(0)e^{i\int_0^t d\tau\delta\omega(\tau)}\rangle e^{-\frac{t}{2T_1}}\right] \tag{16}$$

where $\alpha_{01}(t)$ is the isotropic transition polarizability between the ground (0) and first excited (1) states at a particular time t, and T_1 is the vibrational population lifetime which is estimated from experiment to be 5 ps.[40] $\delta\omega(t) = \omega(t) - \langle\omega\rangle$ tracks the instantaneous frequency fluctuations.

Results & Discussion

A. Molecular Dynamics Simulations

Molecular dynamics simulations of one terminal alkyne molecule (EBA or PAC) solvated in otherwise pure TEA were performed for cubic simulation boxes with an approximately 4 nm edge length. Cylindrical distribution functions (CDFs) were calculated and are shown in Figure 2.
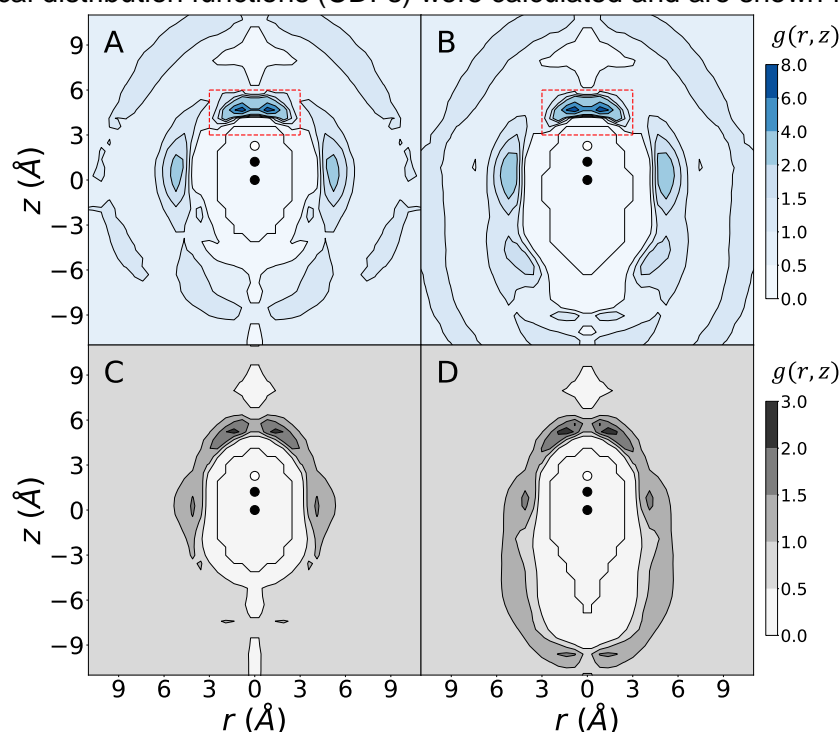

Figure 2: *Cylindrical distribution functions for TEA nitrogen atoms (A and B) or carbon atoms (C and D) with respect to the terminal alkyne moiety of PAC (A and C) or EBA (B and D). The black circle at (0, 0) is the location of the carbon in the terminal alkyne bonded to the R group. This first carbon is triple bonded to the carbon represented by the black circle at about (0, 1.215). The terminal alkyne hydrogen is represented by a white circle at about (0, 2.276). The red box (A and B) highlights the main nitrogen peak. The r axis is reflected for clarity.*

The effect of the substituent to the alkyne molecule on the structure of the solvent is relatively small, especially in the vicinity of the terminal alkyne moiety. There are some interactions between the triple bond and the TEA carbons, which cause peaks in both CDFs since the nitrogens are bound to the carbons. Most significantly, the CDFs clearly show a much stronger interaction between the terminal alkyne and the TEA nitrogen than between the terminal alkyne and the TEA carbons. There is also a small increase in density near the terminal alkyne hydrogen

in the carbon CDFs. These are likely carbons which are bonded to the nitrogens which are directly interacting with the alkyne. The maximum CDF value observed for the nitrogen is about 7.3 for both alkynes, more than two times as much as is observed for the carbons. The largest nitrogen peak occurs near the terminal alkyne hydrogen. It is centered approximately 2 Å from the terminal alkyne hydrogen with an average C-H-N angle of 180 degrees. It begins at approximately 1 Å from the terminal alkyne hydrogen and ends about 5 Å away. The peak is moderately spread out and the absolute maximum of the peak occurs away from its center. If we integrate this major peak between $z = [3, 6]$ and $r = [0, 3]$, (the area inside the red square in Figure 2) we find that it represents an average of 0.57 (0.61) TEA nitrogens near the terminal hydrogen of PAC (EBA). We can also count the number of nitrogen atoms in the same region over the course of our 200 ns simulation where snapshots were collected every 2 ps (Figure 3). For PAC (EBA) 59.0 % (62.7 %) of snapshots have exactly one nitrogen atom in the region of interest, 40.3 % (36.4 %) of snapshots have no nitrogen atoms in that volume, and 0.7 % (0.8 %) of snapshots have 2 nitrogen atoms. No snapshots have three or more nitrogens in the space.

These values are identical to those observed if we analyze our higher resolution 25 ns simulation where snapshots were collected every 0.1 ps. We say that the alkynes in snapshots where there is a nitrogen near the terminal alkyne hydrogen are "nitrogen associated." If there is no TEA nitrogen near the hydrogen, the alkyne is said to be "carbon associated." Because the number of snapshots where 2 or more TEA Ns are present is so small, the values from integration can be interpreted as a measure of the likelihood that the alkyne is nitrogen associated.
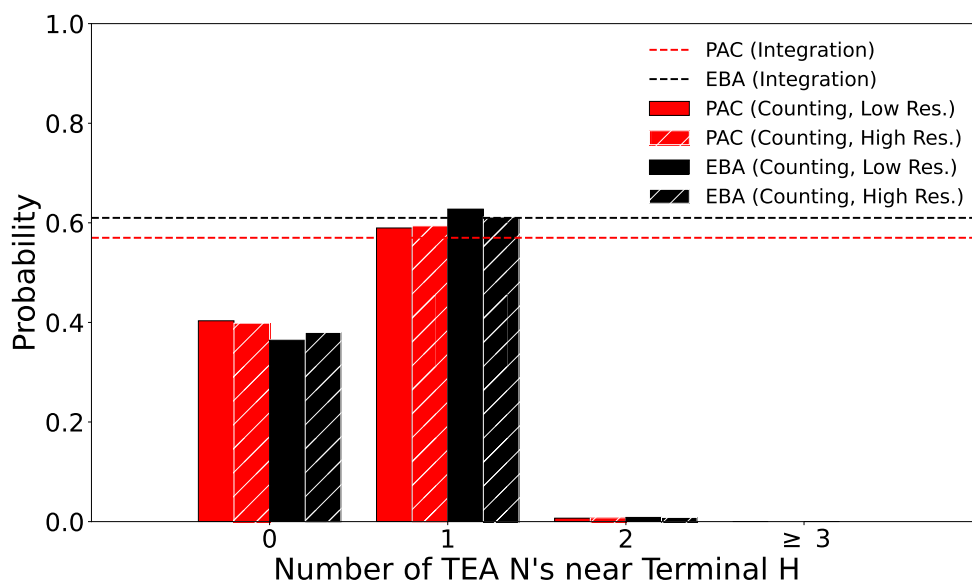

Figure 3: *Probability of finding nitrogen atoms near the terminal alkyne hydrogen, taken by integration of the cylindrical distribution function, and by counting nitrogen atoms near the alkyne hydrogen in low-resolution (snapshots collected every 2 ps) and high-resolution (snapshots collected every 0.1 ps) simulations.*

The fact that neither the sampling resolution nor the length of the simulation changes the apparent probability of nitrogen association for the terminal alkyne implies that the dynamical processes which change the number of nitrogens near the terminal alkyne are relatively slow,

with timescales larger than 2 ps. We believe that the correct molecular picture is one where the alkyne spends significant time interacting with specific nitrogen atoms. After at least 2 ps, the interaction breaks and the alkyne does not interact with any nitrogen for a period of time. This is supported by the small number of cases where two nitrogens are near the terminal alkyne – it is unlikely that nitrogens "compete" to interact with the alkyne. To confirm this, we calculated the time correlation function for the number of nitrogens near the alkyne from our high-resolution simulation and fit it to a tri-exponential function. We then integrated the tri-exponential function to obtain the correlation time. For PAC (EBA), the correlation time was 3.1 ps (3.5 ps), and the longest timescale was 7.4 ps (9.1 ps). We interpret this to mean that the average timescale for alkyne-nitrogen interactions is about 3-4 ps, and the strongest interactions last about 7-10 ps.

B. Dimer Quantum Mechanics:

To understand the effect of the strong TEA nitrogen-alkyne hydrogen interaction on the vibrational frequency, we extracted one TEA-PAC dimer and one TEA-EBA dimer for further analysis using DFT and LNM-DVR based vibrational frequency calculations. The selected dimers initially exhibited nitrogen association (Figure 4). We performed constrained geometry optimizations where the alkyne hydrogen-TEA nitrogen distance (hereafter H-N distance) was constrained to increasing values and computed the terminal alkyne stretching frequencies of the resulting structures. Using ALMO calculations, we decomposed these frequencies into components due to Pauli exclusion, electrostatics, dispersion, polarization, and charge transfer.
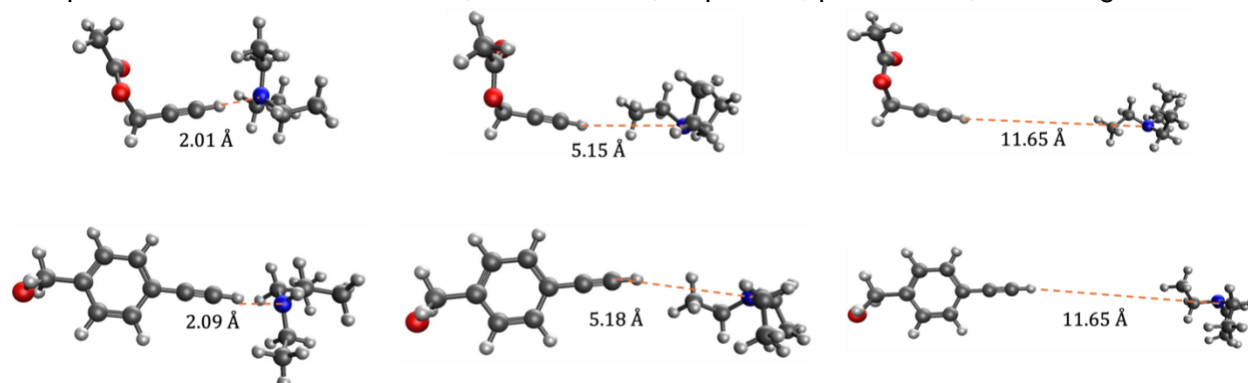

Figure 4: *Optimized TEA/PAC (top row) and TEA/EBA (bottom row) dimers constrained to different H-N distances. (Left column) The fully optimized structures with no constraints. (Middle column) Once there is enough space between the terminal alkyne and the TEA, ethyl groups fill the space and form carbon-associated structures. (Right column) At large distances, the TEA has no effect on the terminal alkyne.*

In Figure 5, the frequency as a function of the H-N distance for three density functional methods are shown. The frequency is relatively low for nitrogen-associated structures, increasing as the distance between the H and N increases. After a H-N distance of about 5 Å, the TEA rotates such that an ethyl fills the space between the TEA and alkyne and the structure becomes carbon-associated. There is little change in the frequency as the H-N distance continues to increase from 5 Å to 12 Å, showing that a carbon-associated alkyne is similar to a gas phase alkyne. Multiple density functionals agree on this trend across both alkyne molecules.

Figure 5 also shows the decomposition of $\Delta\omega_{TEA}$. For the nitrogen-associated structures, Pauli exclusion, charge transfer, and electric field interactions have the largest effect on the frequency. Pauli exclusion tends to increase the frequency, while charge transfer and electrostatics tend to decrease it. The total frequency shift is determined by the balance of these effects – for these optimized structures, the effects which decrease the frequency sum to outweigh the frequency increase from Pauli exclusion. However, a spectroscopic map would need to be flexible enough to capture both of these frequency increasing and frequency decreasing effects, which might be differently balanced in an actual MD simulation.

In this system, both electrostatics and charge transfer can be understood to be related to the excess donatable electron density near the TEA nitrogen. In a nitrogen associated configuration, these electrons create a locus of negative charge near the partially positive terminal alkyne hydrogen (electrostatics) and interact favorably with the weakly Lewis acidic terminal alkyne hydrogen (charge transfer). Both of these effects tend to weaken the C-H bond and thus lower the frequency for the C≡C-H vibration. We would expect them to be strongest when the angle between the terminal alkyne carbon bonded to the terminal hydrogen, the terminal hydrogen, and the TEA nitrogen is 180 degrees. The Pauli exclusion interaction is also related to the presence of electrons. However, we expect their strength to be less dependent on the angle between the alkyne and TEA than electrostatics or charge transfer.
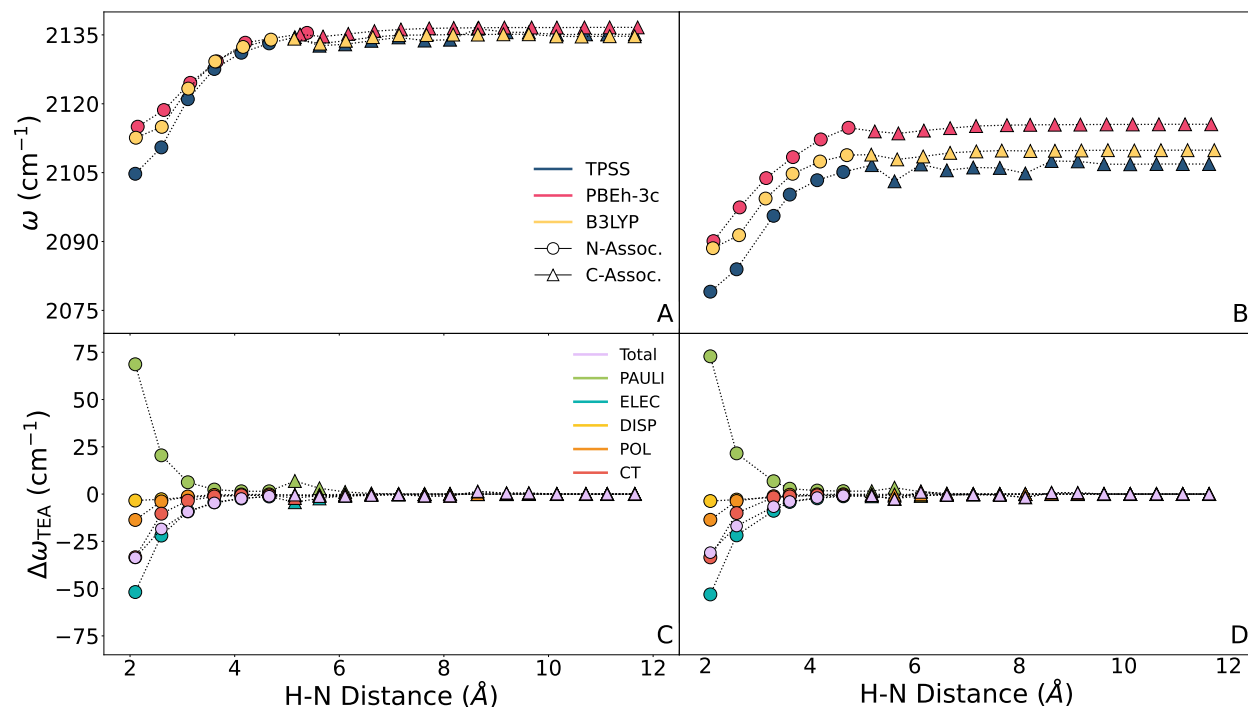

Figure 5: *Frequency (A and B) and decomposition (C and D) as a function of the distance between the TEA nitrogen and the terminal alkyne hydrogen of PAC (A and C) or EBA (B and D). Frequencies (A and B) were calculated with three different methods: B3LYP-D3/def2-TZVPD, TPSS-D3/6-311++G**, and PBEh-3c/def2-mSVP. Decompositions were computed using TPSS-D3/6-311++G**.*

C. Spectroscopic Mapping

From our MD simulations, we know that the nitrogen from TEA interacts strongly with the terminal alkyne hydrogen about half the time. From our DFT calculations, we know that if the TEA nitrogen is interacting with the terminal alkyne hydrogen, then the frequency will decrease compared to carbon-association or the gas phase. How do these effects combine to produce the experimentally observed Raman spectrum?

First, we used 100 of our 1000 snapshots for each alkyne to evaluate the appropriateness of the Condon approximation that the scattering cross section of the vibration is uncorrelated with the vibrational frequency. We find it is valid – the calculated transition polarizabilities have no relationship to the frequencies or to $\Delta\omega_{TEA}$.

Next, we turned to determine good variables for a spectroscopic map. From our ALMO-FDA calculations, we have a good sense of the effects which alter the vibrational frequency of terminal alkynes interacting with TEA molecules – charge transfer, electrostatics, and Pauli exclusion. To build a spectroscopic map for the change in frequency due to the TEA, we need to find items in the MD force field which map well to these effects. Electrostatics and charge transfer may be captured by the electrostatics in the simulation – atoms with strong negative charges in the MD simulation tend to have larger local electron densities. To capture the directionality of these effects, we use the electric field rather than the electric potential. The damped shifted force method was used for these calculations.[41] There is a weak correlation between $\Delta\omega_{TEA}$ and the electric field due to the TEA molecules at the site of the hydrogen atom and pointed in the opposite direction from the H-C bond. However, we find that the quality of the correlation increases if the location the electric field is calculated from is a point 1 Å away from the alkyne hydrogen, along the axis of the C≡C bond. This point is at about $r = 0$ Å and $z = 3.3$ Å on the CDFs in Figure 2. This is inside the area where TEA nitrogens which are near the terminal alkyne hydrogen appear. We also found that the correlation increased even further if the electric field from only nitrogen atoms was included in this calculation, rather than from all TEA atoms. This variable, the electric field from the nitrogens at $r = 0$ Å and $z = 3.3$ Å, captures the electrostatics and charge transfer due to the electron density on the nitrogen atoms. It also likely captures some Pauli exclusion effects as well, since the nitrogen has unusually high electron density.

The Pauli exclusion effect is modeled in the OPLS force field by the repulsive portion of the Lennard-Jones potential. To capture this, we examined the repulsive part of the Lennard-Jones potential at each atom in the terminal alkyne moiety – the triple bonded carbons and the terminal hydrogen. The repulsions were calculated by summing the interactions of all non-nitrogen atoms, to avoid double counting information already present in the electric field. By themselves, the correlations of each of these repulsive Lennard-Jones variables to $\Delta\omega_{TEA}$ are small. However, when added through multilinear regression to the electric field, the overall correlation with $\Delta\omega_{TEA}$ increases significantly. We also tested the attractive Lennard-Jones potential, but the performance was worse or no better depending on exactly how these interactions were added to the model.

Table 1: *Multilinear regression vibrational spectroscopic map for the frequency change due to the TEA solvent. H refers to the terminal hydrogen, CH refers to the triple bonded carbon also bound to the terminal hydrogen, and CR refers to the triple bonded carbon also bound to the R group. The coefficients were determined using a randomly selected ¾ of the 2,000 snapshots of both*

alkynes in TEA. Uncertainty in the coefficients was estimated by fitting 25 randomly selected ¾ training sets and finding the 95 % confidence interval of the mean of the coefficients found with these training sets. The final digit shown in each entry in the table below is uncertain.

Symbol	Coefficient Value	PAC $\langle \Delta\omega \rangle$ (cm^{-1})	PAC $\sigma_{\Delta\omega}$ (cm^{-1})	EBA $\langle \Delta\omega \rangle$ (cm^{-1})	EBA $\sigma_{\Delta\omega}$ (cm^{-1})
a	3.89 x 10^{-10} V^{-1} m cm^{-1}	-3.30	3.32	-3.32	3.29
b_H	1.57 x 10^{-1} kJ^{-1} mol cm^{-1}	2.46	2.01	2.45	1.97
b_{CH}	7 x 10^{-2} kJ^{-1} mol cm^{-1}	0.2	0.1	0.2	0.1
b_{CR}	-3.4 x 10^{-1} kJ^{-1} mol cm^{-1}	-0.61	0.30	-0.56	0.27

Our final map is based on multilinear regression of the variables described above. As an equation, it is

$$\omega = \omega_g + \Delta\omega(\theta_{RCC}, \theta_{HCC}) + a\hat{r}_{CR \equiv CH} \cdot \left(\sum_{n=1}^{N} \vec{E}_{Hn} \right) + \sum_{i=1}^{3} \left(b_i \sum_{m=1}^{M} 4\varepsilon_m \left(\frac{\sigma_m}{r_{mi}} \right)^{12} \right) \qquad (17)$$

where n iterates over all N nitrogen atoms, $\vec{E}_{Hn}$ is the contribution to the electric field near the terminal hydrogen, as described above, $\hat{r}_{CR \equiv CH}$ is the unit vector pointing from the triple bonded carbon bound to the R group to the triple bonded carbon bound to the terminal hydrogen, and a is a coefficient found through multilinear regression. In the second term, i iterates over the three terminal alkyne atoms (C≡C-H), each of which has been assigned a coefficient b_i by multilinear regression. m iterates over all M non-nitrogen solvent atoms, ε_m and σ_m are the Lennard-Jones coefficients for that atom (no mixing rules were used) and r_{mi} is the distance between solvent atom m and terminal alkyne atom i. To obtain the complete frequency ω, we also add the gas phase frequency ω_g (2138.39 cm^{-1} for PAC and 2110.65 cm^{-1} for EBA) and the angle effect $\Delta\omega(\theta_{RCC}, \theta_{HCC})$ based on a smooth bivariate spline approximation to gas phase data. The values of the coefficients are given in Table 1. We do not include an intercept term in our regression model, since $\Delta\omega_{TEA} = 0$ cm^{-1} in the absence of TEA solvent.

Table 1 also shows the average and standard deviation change to the frequency for each variable. As expected, the electric field near the terminal hydrogen tends to decrease the frequency, likely when nitrogen associated, but can also easily contribute nothing to the frequency, likely when carbon-associated. The repulsive Lennard-Jones potential at the terminal hydrogen increases the frequency in nearly all cases, as expected. The repulsive Lennard-Jones potentials at the carbons provide more modest and less variant changes to the frequency.

Evaluated against our 500-member two-alkyne test set, this map had a correlation coefficient of 0.74 with a root mean squared error of 2.61 cm^{-1} (Figure 6). Similar statistics and coefficients are obtained if maps are created and tested with one-alkyne datasets instead of two-alkyne datasets. We tested several other types of regression model including artificial neural networks. All performed no better than multilinear regression. Artificial neural networks which were too small struggled to learn anything from the training set; networks which were only slightly larger tended to strongly overfit the training data and fail against the test set. Because our correlation is smaller than is ideal, there is variance in $\Delta\omega_{TEA}$ that is not captured by the map.

Thus, we expect that the frequency distributions and Raman spectra calculated using it will have smaller widths than are observed in experiment.
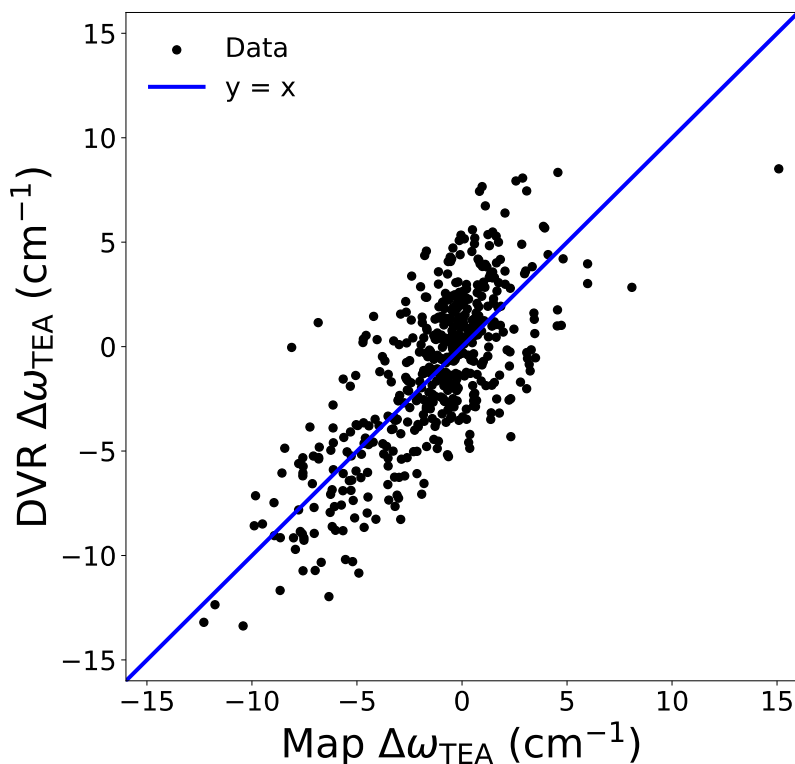

Figure 6: *Performance of the spectroscopic map developed in this work to compute the effect of the solvent on the alkyne probe frequency. The blue line representing a perfect correlation is provided for comparison. The correlation between map frequencies and DVR frequencies is 0.74 and the root-mean-squared-difference is 2.61 cm^{-1}.*

D. Computational Raman Spectra

With this map in hand, we performed MD simulations of each alkyne in TEA for 25 ns where snapshots were collected every 0.1 ps. The map variables were extracted from this simulation and map frequencies were computed for every snapshot. This frequency trajectory was used to compute Raman spectra according to the fluctuating frequency approximation (Eq. 16). These Raman spectra and the underlying frequency distributions are shown in Figure 7.
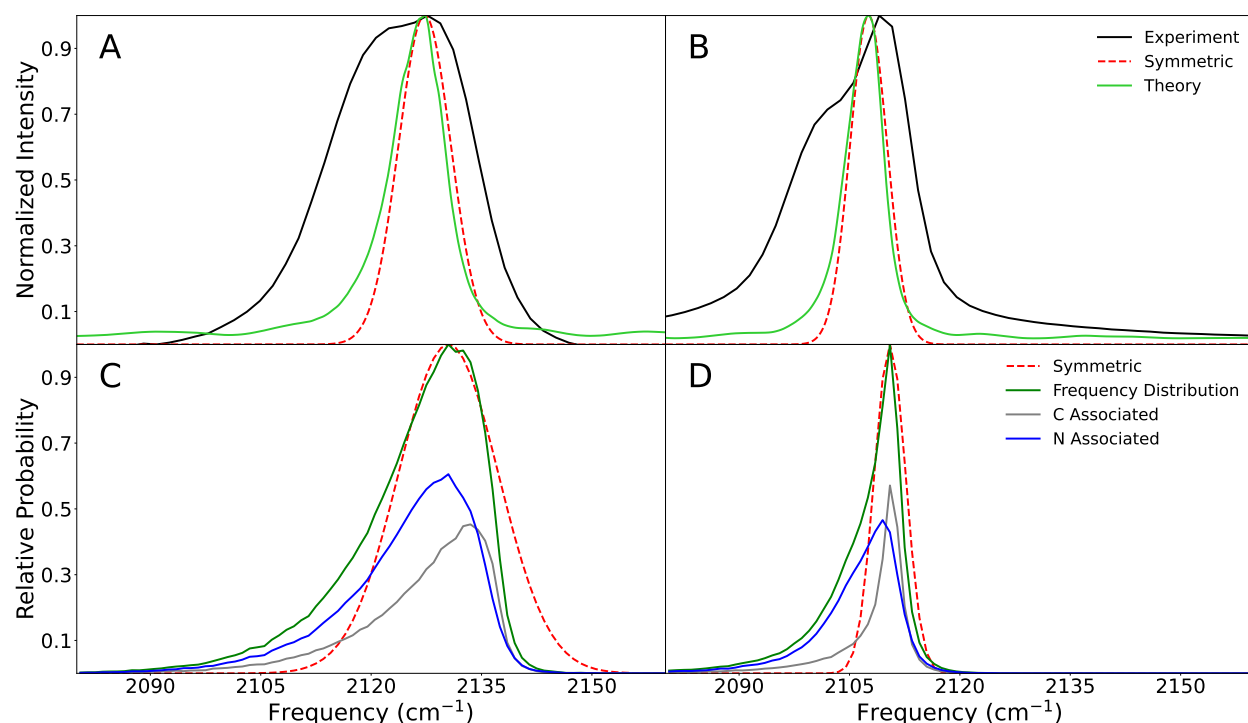
Figure 7: *Raman spectra and frequency distributions computed using the spectroscopic map for PAC (A and C) and EBA (B and D). (A and B) Experimental[β] and computational Raman spectra. The dotted red curve is a completely symmetric Gaussian function with the same FWHM and peak frequency as the computational spectrum. (C and D) The computational frequency histograms, broken down into nitrogen associated and carbon associated populations. The dotted red curve is a completely symmetric Gaussian function with the same FWHM and peak frequency as the full distribution.*

Our computed Raman spectra are significantly narrower than experiment, likely because we have removed R group effects from the frequency distributions and because our map misses some of the frequency variance from DFT. One of the most interesting features of the experimental spectra is their pronounced asymmetry. Our spectra are also asymmetric, as can be seen by comparison to a fully symmetric Gaussian distribution with the same peak location and full-width-at-half-maximum as our calculated spectra. In particular, they are broadened to the left, like the experimental spectra.

To determine the origin of the asymmetry in the computed spectra, we examine the underlying frequency distributions. These are also asymmetric, and this asymmetry arises for two reasons. First, bending of the CCH and CCC angles of the alkyne tend to reduce the frequency. However, this likely does not explain the experimental asymmetry. This angle effect would show up in the experiment as a hot band at lower frequencies, and the intensity of this band would increase with temperature. However, the experiments show a decrease or no change in the left side of the spectrum with an increase in temperature.

Second, interaction with nitrogen reduces the frequency. The frequency distribution has been broken down into nitrogen-associated and carbon-associated populations in Figure 7C and Figure 7D. For both alkynes, the nitrogen-associated population has a lower average frequency.

When put together with the carbon associated population, we obtain a left-broadened spectrum like the experiment.

Conclusion

Together, this computational and experimental evidence clearly shows that association with the electron dense nitrogen creates a population of low frequency terminal alkynes which show up in the experimental spectrum as a shoulder. We predict that these associations are relatively long lasting, on the order of 3-10 ps. This is similar to the persistence of hydrogen bonds in water.[42] The overall free energy for the terminal alkyne existing in the electron rich and electron poor environments is nearly equal, with a small preference for the electron rich environment. However, the frequency is less variant in the electron poor environment, leading to a sharper peak in that population. Our results imply that the center frequency of the alkynes reports on the availability of such electron rich environments.

Acknowledgments

References

(1) Baiz, C. R.; Błasiak, B.; Bredenbeck, J.; Cho, M.; Choi, J.-H.; Corcelli, S. A.; Dijkstra, A. G.; Feng, C.-J.; Garrett-Roe, S.; Ge, N.-H.; Hanson-Heine, M. W. D.; Hirst, J. D.; Jansen, T. L. C.; Kwac, K.; Kubarych, K. J.; Londergan, C. H.; Maekawa, H.; Reppert, M.; Saito, S.; Roy, S.; Skinner, J. L.; Stock, G.; Straub, J. E.; Thielges, M. C.; Tominaga, K.; Tokmakoff, A.; Torii, H.; Wang, L.; Webb, L. J.; Zanni, M. T. Vibrational Spectroscopic Map, Vibrational Spectroscopy, and Intermolecular Interaction. *Chem. Rev.* **2020**, *120* (15), 7152–7218. https://doi.org/10.1021/acs.chemrev.9b00813.

(2) Xu, R. J.; Blasiak, B.; Cho, M.; Layfield, J. P.; Londergan, C. H. A Direct, Quantitative Connection between Molecular Dynamics Simulations and Vibrational Probe Line Shapes. *J. Phys. Chem. Lett.* **2018**, *9* (10), 2560–2567. https://doi.org/10.1021/acs.jpclett.8b00969.

(3) Begušić, T.; Blake, G. A. Two-Dimensional Infrared-Raman Spectroscopy as a Probe of Water's Tetrahedrality. *Nat Commun* **2023**, *14* (1), 1950. https://doi.org/10.1038/s41467-023-37667-7.

(4) Fujioka, H.; Shou, J.; Kojima, R.; Urano, Y.; Ozeki, Y.; Kamiya, M. Multicolor Activatable Raman Probes for Simultaneous Detection of Plural Enzyme Activities. *J. Am. Chem. Soc.* **2020**, *142* (49), 20701–20707. https://doi.org/10.1021/jacs.0c09200.

(5) Schneider, S. H.; Boxer, S. G. Vibrational Stark Effects of Carbonyl Probes Applied to Reinterpret IR and Raman Data for Enzyme Inhibitors in Terms of Electric Fields at the Active Site. *J. Phys. Chem. B* **2016**, *120* (36), 9672–9684. https://doi.org/10.1021/acs.jpcb.6b08133.

(6) Tian, S.; Li, H.; Li, Z.; Tang, H.; Yin, M.; Chen, Y.; Wang, S.; Gao, Y.; Yang, X.; Meng, F.; Lauher, J. W.; Wang, P.; Luo, L. Polydiacetylene-Based Ultrastrong Bioorthogonal Raman Probes for Targeted Live-Cell Raman Imaging. *Nat Commun* **2020**, *11* (1), 81. https://doi.org/10.1038/s41467-019-13784-0.

(7) Gruenbaum, S. M.; Tainter, C. J.; Shi, L.; Ni, Y.; Skinner, J. L. Robustness of Frequency, Transition Dipole, and Coupling Maps for Water Vibrational Spectroscopy. *J. Chem. Theory Comput.* **2013**, *9* (7), 3109–3117. https://doi.org/10.1021/ct400292q.

(8) Romei, M. G.; von Krusenstiern, E. V.; Ridings, S. T.; King, R. N.; Fortier, J. C.; McKeon, C. A.; Nichols, K. M.; Charkoudian, L. K.; Londergan, C. H. Frequency Changes in Terminal Alkynes Provide Strong, Sensitive, and Solvatochromic Raman Probes of Biochemical Environments. *J. Phys. Chem. B* **2023**, *127* (1), 85–94. https://doi.org/10.1021/acs.jpcb.2c06176.

(9) Bi, X.; Miao, K.; Wei, L. Alkyne-Tagged Raman Probes for Local Environmental Sensing by Hydrogen–Deuterium Exchange. *J. Am. Chem. Soc.* **2022**, *144* (19), 8504–8514. https://doi.org/10.1021/jacs.2c01991.

(10) Dong, T.; Yu, P.; Zhao, J.; Wang, J. Probing the Local Structure and Dynamics of Nucleotides Using Vibrationally Enhanced Alkynyl Stretching. *Phys. Chem. Chem. Phys.* **2022**, *24* (48), 29988–29998. https://doi.org/10.1039/D2CP03920F.

(11) Epstein, S. C.; Huff, A. R.; Winesett, E. S.; Londergan, C. H.; Charkoudian, L. K. Tracking Carrier Protein Motions with Raman Spectroscopy. *Nat Commun* **2019**, *10* (1), 2227. https://doi.org/10.1038/s41467-019-10184-2.

(12) Błasiak, B.; Londergan, C. H.; Webb, L. J.; Cho, M. Vibrational Probes: From Small Molecule Solvatochromism Theory and Experiments to Applications in Complex Systems. *Acc. Chem. Res.* **2017**, *50* (4), 968–976. https://doi.org/10.1021/acs.accounts.7b00002.

(13) Dodo, K.; Fujita, K.; Sodeoka, M. Raman Spectroscopy for Chemical Biology Research. *J. Am. Chem. Soc.* **2022**, *144* (43), 19651–19667. https://doi.org/10.1021/jacs.2c05359.

(14) Streu, K.; Hunsberger, S.; Patel, J.; Wan, X.; Daly, C. A., Jr. Development of a Universal Method for Vibrational Analysis of the Terminal Alkyne C≡C Stretch. *The Journal of Chemical Physics* **2024**, *160* (7), 074106. https://doi.org/10.1063/5.0185580.

(15) Epifanovsky, E.; Gilbert, A. T. B.; Feng, X.; Lee, J.; Mao, Y.; Mardirossian, N.; Pokhilko, P.; White, A. F.; Coons, M. P.; Dempwolff, A. L.; Gan, Z.; Hait, D.; Horn, P. R.; Jacobson, L. D.; Kaliman, I.; Kussmann, J.; Lange, A. W.; Lao, K. U.; Levine, D. S.; Liu, J.; McKenzie, S. C.; Morrison, A. F.; Nanda, K. D.; Plasser, F.; Rehn, D. R.; Vidal, M. L.; You, Z.-Q.; Zhu, Y.; Alam, B.; Albrecht, B. J.; Aldossary, A.; Alguire, E.; Andersen, J. H.; Athavale, V.; Barton, D.; Begam, K.; Behn, A.; Bellonzi, N.; Bernard, Y. A.; Berquist, E. J.; Burton, H. G. A.; Carreras, A.; Carter-Fenk, K.; Chakraborty, R.; Chien, A. D.; Closser, K. D.; Cofer-Shabica, V.; Dasgupta, S.; de Wergifosse, M.; Deng, J.; Diedenhofen, M.; Do, H.; Ehlert, S.; Fang, P.-T.; Fatehi, S.; Feng, Q.; Friedhoff, T.; Gayvert, J.; Ge, Q.; Gidofalvi, G.; Goldey, M.; Gomes, J.; González-Espinoza, C. E.; Gulania, S.; Gunina, A. O.; Hanson-Heine, M. W. D.; Harbach, P. H. P.; Hauser, A.; Herbst, M. F.; Hernández Vera, M.; Hodecker, M.; Holden, Z. C.; Houck, S.; Huang, X.; Hui, K.; Huynh, B. C.; Ivanov, M.; Jász, Á.; Ji, H.; Jiang, H.; Kaduk, B.; Kähler, S.; Khistyaev, K.; Kim, J.; Kis, G.; Klunzinger, P.; Koczor-Benda, Z.; Koh, J. H.; Kosenkov, D.; Koulias, L.; Kowalczyk, T.; Krauter, C. M.; Kue, K.; Kunitsa, A.; Kus, T.; Ladjánszki, I.; Landau, A.; Lawler, K. V.; Lefrancois, D.; Lehtola, S.; Li, R. R.; Li, Y.-P.; Liang, J.; Liebenthal, M.; Lin, H.-H.; Lin, Y.-S.; Liu, F.; Liu, K.-Y.; Loipersberger, M.; Luenser, A.; Manjanath, A.; Manohar, P.; Mansoor, E.; Manzer, S. F.; Mao, S.-P.; Marenich, A. V.; Markovich, T.; Mason, S.; Maurer, S. A.; McLaughlin, P.

F.; Menger, M. F. S. J.; Mewes, J.-M.; Mewes, S. A.; Morgante, P.; Mullinax, J. W.; Oosterbaan, K. J.; Paran, G.; Paul, A. C.; Paul, S. K.; Pavošević, F.; Pei, Z.; Prager, S.; Proynov, E. I.; Rák, Á.; Ramos-Cordoba, E.; Rana, B.; Rask, A. E.; Rettig, A.; Richard, R. M.; Rob, F.; Rossomme, E.; Scheele, T.; Scheurer, M.; Schneider, M.; Sergueev, N.; Sharada, S. M.; Skomorowski, W.; Small, D. W.; Stein, C. J.; Su, Y.-C.; Sundstrom, E. J.; Tao, Z.; Thirman, J.; Tornai, G. J.; Tsuchimochi, T.; Tubman, N. M.; Veccham, S. P.; Vydrov, O.; Wenzel, J.; Witte, J.; Yamada, A.; Yao, K.; Yeganeh, S.; Yost, S. R.; Zech, A.; Zhang, I. Y.; Zhang, X.; Zhang, Y.; Zuev, D.; Aspuru-Guzik, A.; Bell, A. T.; Besley, N. A.; Bravaya, K. B.; Brooks, B. R.; Casanova, D.; Chai, J.-D.; Coriani, S.; Cramer, C. J.; Cserey, G.; DePrince, A. E., III; DiStasio, R. A., Jr.; Dreuw, A.; Dunietz, B. D.; Furlani, T. R.; Goddard, W. A., III; Hammes-Schiffer, S.; Head-Gordon, T.; Hehre, W. J.; Hsu, C.-P.; Jagau, T.-C.; Jung, Y.; Klamt, A.; Kong, J.; Lambrecht, D. S.; Liang, W.; Mayhall, N. J.; McCurdy, C. W.; Neaton, J. B.; Ochsenfeld, C.; Parkhill, J. A.; Peverati, R.; Rassolov, V. A.; Shao, Y.; Slipchenko, L. V.; Stauch, T.; Steele, R. P.; Subotnik, J. E.; Thom, A. J. W.; Tkatchenko, A.; Truhlar, D. G.; Van Voorhis, T.; Wesolowski, T. A.; Whaley, K. B.; Woodcock, H. L., III; Zimmerman, P. M.; Faraji, S.; Gill, P. M. W.; Head-Gordon, M.; Herbert, J. M.; Krylov, A. I. Software for the Frontiers of Quantum Chemistry: An Overview of Developments in the Q-Chem 5 Package. *The Journal of Chemical Physics* **2021**, *155* (8), 084801. https://doi.org/10.1063/5.0055522.

(16) Becke, A. D. Density-functional Thermochemistry. III. The Role of Exact Exchange. *The Journal of Chemical Physics* **1993**, *98* (7), 5648–5652. https://doi.org/10.1063/1.464913.

(17) Binkley, J. S.; Pople, J. A.; Hehre, W. J. Self-Consistent Molecular Orbital Methods. 21. Small Split-Valence Basis Sets for First-Row Elements. *J. Am. Chem. Soc.* **1980**, *102* (3), 939–947. https://doi.org/10.1021/ja00523a008.

(18) Grimme, S.; Brandenburg, J. G.; Bannwarth, C.; Hansen, A. Consistent Structures and Interactions by Density Functional Theory with Small Atomic Orbital Basis Sets. *The Journal of Chemical Physics* **2015**, *143* (5), 054107. https://doi.org/10.1063/1.4927476.

(19) Grimme, S.; Ehrlich, S.; Goerigk, L. Effect of the Damping Function in Dispersion Corrected Density Functional Theory. *Journal of Computational Chemistry* **2011**, *32* (7), 1456–1465. https://doi.org/10.1002/jcc.21759.

(20) Tao, J.; Perdew, J. P.; Staroverov, V. N.; Scuseria, G. E. Climbing the Density Functional Ladder: Nonempirical Meta–Generalized Gradient Approximation Designed for Molecules and Solids. *Phys. Rev. Lett.* **2003**, *91* (14), 146401. https://doi.org/10.1103/PhysRevLett.91.146401.

(21) Colbert, D. T.; Miller, W. H. A Novel Discrete Variable Representation for Quantum Mechanical Reactive Scattering via the S-matrix Kohn Method. *J. Chem. Phys.* **1992**, *96* (3), 1982–1991. https://doi.org/10.1063/1.462100.

(22) Horn, P. R.; Mao, Y.; Head-Gordon, M. Probing Non-Covalent Interactions with a Second Generation Energy Decomposition Analysis Using Absolutely Localized Molecular Orbitals. *Phys. Chem. Chem. Phys.* **2016**, *18* (33), 23067–23079. https://doi.org/10.1039/C6CP03784D.

(23) Khaliullin, R. Z.; Cobar, E. A.; Lochan, R. C.; Bell, A. T.; Head-Gordon, M. Unravelling the Origin of Intermolecular Interactions Using Absolutely Localized Molecular Orbitals. *Journal of Physical Chemistry A* **2007**, *111* (36), 8753–8765. https://doi.org/10.1021/jp073685z.

(24) Corcelli, S. A.; Skinner, J. L. Infrared and Raman Line Shapes of Dilute HOD in Liquid H_2O and D_2O from 10 to 90 °C. *J. Phys. Chem. A* **2005**, *109* (28), 6154–6165. https://doi.org/10.1021/jp0506540.

(25) Daly, C. A.; Streacker, L. M.; Sun, Y.; Pattenaude, S. R.; Hassanali, A. A.; Petersen, P. B.; Corcelli, S. A.; Ben-Amotz, D. Decomposition of the Experimental Raman and Infrared Spectra of Acidic Water into Proton, Special Pair, and Counterion Contributions. *J. Phys. Chem. Lett.* **2017**, *8* (21), 5246–5252. https://doi.org/10.1021/acs.jpclett.7b02435.

(26) Eastman, P.; Swails, J.; Chodera, J. D.; McGibbon, R. T.; Zhao, Y.; Beauchamp, K. A.; Wang, L.-P.; Simmonett, A. C.; Harrigan, M. P.; Stern, C. D.; Wiewiora, R. P.; Brooks, B. R.; Pande, V. S. OpenMM 7: Rapid Development of High Performance Algorithms for Molecular Dynamics. *PLOS Computational Biology* **2017**, *13* (7), e1005659. https://doi.org/10.1371/journal.pcbi.1005659.

(27) Martyna, G. J.; Klein, M. L.; Tuckerman, M. Nosé–Hoover Chains: The Canonical Ensemble via Continuous Dynamics. *The Journal of Chemical Physics* **1992**, *97* (4), 2635–2643. https://doi.org/10.1063/1.463940.

(28) Chow, K.-H.; Ferguson, D. M. Isothermal-Isobaric Molecular Dynamics Simulations with Monte Carlo Volume Sampling. *Computer Physics Communications* **1995**, *91* (1), 283–289. https://doi.org/10.1016/0010-4655(95)00059-O.

(29) Martínez, L.; Andrade, R.; Birgin, E. G.; Martínez, J. M. PACKMOL: A Package for Building Initial Configurations for Molecular Dynamics Simulations. *J Comput Chem* **2009**, *30* (13), 2157–2164. https://doi.org/10.1002/jcc.21224.

(30) Essmann, U.; Perera, L.; Berkowitz, M. L.; Darden, T.; Lee, H.; Pedersen, L. G. A Smooth Particle Mesh Ewald Method. *The Journal of Chemical Physics* **1995**, *103* (19), 8577–8593. https://doi.org/10.1063/1.470117.

(31) Jorgensen, W. L.; Maxwell, D. S.; Tirado-Rives, J. Development and Testing of the OPLS All-Atom Force Field on Conformational Energetics and Properties of Organic Liquids. *J. Am. Chem. Soc.* **1996**, *118* (45), 11225–11236. https://doi.org/10.1021/ja9621760.

(32) Rego, T.; Silva, G. M. C.; Goldmann, M.; Filipe, E. J. M.; Morgado, P. Optimized All-Atom Force Field for Alkynes within the OPLS-AA Framework. *Fluid Phase Equilibria* **2022**, *554*, 113314. https://doi.org/10.1016/j.fluid.2021.113314.

(33) Dodda, L. S.; Cabeza de Vaca, I.; Tirado-Rives, J.; Jorgensen, W. L. LigParGen Web Server: An Automatic OPLS-AA Parameter Generator for Organic Ligands. *Nucleic Acids Research* **2017**, *45* (W1), W331–W336. https://doi.org/10.1093/nar/gkx312.

(34) Breneman, C. M.; Wiberg, K. B. Determining Atom-Centered Monopoles from Molecular Electrostatic Potentials. The Need for High Sampling Density in Formamide Conformational Analysis. *Journal of Computational Chemistry* **1990**, *11* (3), 361–373. https://doi.org/10.1002/jcc.540110311.

(35) Adamo, C.; Barone, V. Toward Reliable Density Functional Methods without Adjustable Parameters: The PBE0 Model. *The Journal of Chemical Physics* **1999**, *110* (13), 6158–6170. https://doi.org/10.1063/1.478522.

(36) McGibbon, R. T.; Beauchamp, K. A.; Harrigan, M. P.; Klein, C.; Swails, J. M.; Hernández, C. X.; Schwantes, C. R.; Wang, L.-P.; Lane, T. J.; Pande, V. S. MDTraj: A Modern Open Library for the Analysis of Molecular Dynamics Trajectories. *Biophysical Journal* **2015**, *109* (8), 1528–1532. https://doi.org/10.1016/j.bpj.2015.08.015.

(37) Brinzer, T.; Daly, C. A.; Allison, C.; Garrett-Roe, S.; Corcelli, S. A. Modeling Carbon Dioxide Vibrational Frequencies in Ionic Liquids: III. Dynamics and Spectroscopy. *J. Phys. Chem. B* **2018**, *122* (38), 8931–8942. https://doi.org/10.1021/acs.jpcb.8b05659.

(38) Daly, C. A.; Brinzer, T.; Allison, C.; Garrett-Roe, S.; Corcelli, S. A. Enthalpic Driving Force for the Selective Absorption of CO2 by an Ionic Liquid. *J. Phys. Chem. Lett.* **2018**, *9* (6), 1393–1397. https://doi.org/10.1021/acs.jpclett.8b00347.

(39) Jones, E.; Oliphant, T.; Peterson, P.; others. {SciPy}: Open Source Scientific Tools for {Python}.

(40) Schmidt, J. R.; Corcelli, S. A. Infrared Absorption Line Shapes in the Classical Limit: A Comparison of the Classical Dipole and Fluctuating Frequency Approximations. *The Journal of Chemical Physics* **2008**, *128* (18), 184504. https://doi.org/10.1063/1.2917349.

(41) Fennell, C. J.; Gezelter, J. D. Is the Ewald Summation Still Necessary? Pairwise Alternatives to the Accepted Standard for Long-Range Electrostatics. *Journal of Chemical Physics* **2006**, *124* (23). https://doi.org/10.1063/1.2206581.

(42) Liu, J.; He, X.; Zhang, J. Z. H.; Qi, L.-W. Hydrogen-Bond Structure Dynamics in Bulk Water: Insights from Ab Initio Simulations with Coupled Cluster Theory. *Chem. Sci.* **2018**, *9* (8), 2065–2073. https://doi.org/10.1039/C7SC04205A.